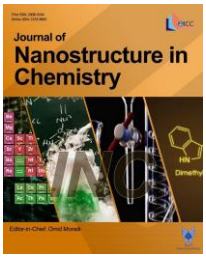

J. Nanostruct Chem. 2026; 16(3): 267-283

Journal of Nanostructure in Chemistry (JNSC)

https://doi.org/10.57647/jnsc.2026.1603.13

Research Article

Engineering Gold Nanocluster/Polymer Hybrid Nanocarriers to Boost Doxorubicin Transport and Cellular Uptake in Gastric Cancer Cells

Yong He[1, *], Jinshi Chen[1], Cheng-San Wong[2]

[1]*R&D Department of 3D Printing, Department of Gastrointestinal Surgery, Digestive Medicine Center, The Seventh Affiliated Hospital, Sun Yat-sen University, Shenzhen 518107, China*

[2] *School of Medicine, Sun Yat-sen University, Shenzhen 518107, China*

[*] **Corresponding authors:** heyong23@mail.sysu.edu.cn

Article History:

Received:
17 December 2025

Revised:
27 January 2026

Accepted:
12 February 2026

Published in Issue:
30 June 2026

Abstract

A pH-responsive, fluorescence-traceable core–shell nanosystem was prepared by co-encapsulating bovine serum albumin–templated Au nanoclusters and doxorubicin within ionotropically crosslinked chitosan (TPP gelation) to enhance intracellular chemotherapy delivery. Formulation screening (CS:TPP 3:1–6:1) identified an optimal composition with a hydrodynamic diameter of 145 ± 5 nm, PDI 0.18, and a surface potential of +32.4 ± 1.2 mV; TEM resolved 2.1 ± 0.3 nm clusters and uniform spherical particles. The lyophilized carriers displayed mesoporosity (SBET 42.5 m2/g; pore volume 0.15 cm3/g; mean pore size 12.4 nm). High drug incorporation was achieved (encapsulation efficiency 82.3 ± 1.4%; loading capacity 12.6 ± 0.8%). Dialysis experiments revealed gated release, with ~22% (pH 7.4) versus ~65% (pH 5.0) at 24 h and ~35% versus ~88% at 72 h; acidic kinetics followed the Korsmeyer–Peppas model (R^2 = 0.985; n = 0.65). Hemolysis remained 1.2% at 100 µg/mL and <3.0% at 1000 µg/mL, and blank carriers preserved >90% viability at 500 µg/mL. In MGC-803 and SGC-7901 cells, the formulation lowered 48 h IC_{50} from 1.85 ± 0.12 to 0.92 ± 0.08 µg/mL and from 2.10 ± 0.15 to 1.15 ± 0.10 µg/mL, respectively. Uptake quantification showed a 4 h mean fluorescence intensity of 717 a.u. versus 280 a.u. for free drug, and apoptosis increased to 59.0% (early apoptosis 35.6%) compared with 40.6% (22.1%) for free drug. Confocal imaging showed time-dependent cytoplasmic-to-nuclear redistribution with persistent cluster fluorescence, supporting tracking. Together, these results suggest that enhanced cell-surface association driven by the cationic shell, combined with endo/lysosomal acidification–triggered reler exposure while limiting premature leakage under physiological pH.

Keywords: Adsorptive endocytosis; Flow cytometry; Ionic gelation; Mesoporous texture; PH-gated diffusion

Cite this article: Yong H., Jinshi Ch., Cheng-San W. Engineering Gold Nanocluster/Polymer Hybrid Nanocarriers to Boost Doxorubicin Transport and Cellular Uptake in Gastric Cancer Cells . *J Nanostruct Chem* **16**, 267-283 (2026). https://doi.org/10.57647/jnsc.2026.1603.13

1. Introduction

Gastric cancer remains a formidable challenge in global oncology, ranking as the fifth most common malignancy and the fourth leading cause of cancer-related mortality worldwide [1]. Despite advancements in surgical interventions and adjuvant therapies, the prognosis for patients with advanced or metastatic gastric cancer is often poor, characterized by low five-year survival rates and high recurrence frequencies [2]. The heterogeneity of

the disease, combined with late-stage diagnosis, necessitates robust systemic therapeutic strategies [3]. Doxorubicin (DOX), an anthracycline antibiotic, serves as a cornerstone chemotherapeutic agent in the management of gastric carcinoma [4]. Its mechanism of action involves the intercalation into DNA base pairs and the inhibition of topoisomerase II [5], leading to the arrest of the cell cycle and the induction of apoptosis [6]. However, the clinical efficacy of DOX is severely compromised by its non-specific biodistribution [7]. The requisite high dosages often precipitate severe off-target toxicities, most notably dose-dependent cardiotoxicity, myelosuppression, and nephrotoxicity, which limit the therapeutic window and compromise patient quality of life [8]. Furthermore, therapeutic outcomes can be attenuated by delivery-related barriers that limit intracellular drug exposure, including non-specific biodistribution, dose-limiting toxicities, and inefficient cellular internalization and trafficking [9,10]. While multidrug resistance mediated by efflux transporters (e.g., ATP-binding cassette family proteins) is an important clinical challenge, the present study does not include resistance-model experiments; therefore, we focus on engineering a nanocarrier strategy to enhance DOX transport and cellular uptake in gastric cancer cells [11].

To circumvent these physiological and cellular barriers, the field of nanomedicine has pivoted towards the development of engineered nanocarriers. Recent reviews further emphasize that rational nanocarrier engineering is increasinglnt constraints such as systemic toxicity, delivery efficiency, and the need for integrated diagnostic readouts (theranostics), rather than payload transport alone In this context, contemporary overviews of nanotechnology-enabled delivery and theranostic paradigms provide an updated framework for designing multifunctional systems that couple imaging/traceability with controlled drug release [12]. These systems aim to exploit the enhanced permeability and retention effect, a phenomenon where the leaky vasculature and impaired lymphatic drainage of solid tumors allow for the passive accumulation of varying nanostructures [13]. Among the plethora of nanomaterials investigated, gold-based nanostructures have garnered significant attention due to their biocompatibility, ease of surface functionalization, and unique optoelectronic properties [14].

Specifically, ultra-small gold nanoclusters (AuNCs), consisting of a few to roughly a hundred gold atoms with a core size smaller than 2 nm, occupy the transition regime between atomic and bulk properties [15]. Unlike larger plasmonic gold nanoparticles (>3 nm) that exhibit localized surface plasmon resonance, AuNCs possess discrete electronic energy levels comparable to the Fermi wavelength of electrons (~0.5 nm), resulting in molecule-like behavior [16,17]. This quantum confinement endows AuNCs with intrinsic, tunable photoluminescence, large Stokes shifts, and high photostability, making them attractive alternatives to conventional organic dyes or toxic semiconductor quantum dots for bioimaging and traceable drurtantly, recent cancer-focused analyses of AuNCs highlight their emerging value as multifunctional components that can simultaneously support imaging/diagnosis and therapeutic payload delivery, thereby accelerating the development of AuNC-based theranostic nanomedicines [18].

Bovine serum albumin (BSA), a widely available and biocompatible protein, has been successfully employed as a template for the biomimetic synthesis of AuNCs [19]. The "one-pot" biomineralization strategy utilizes the reducing capability of tyrosine residues and the stabilizing potential of cysteine thiols within the BSA structure to sequester and reduce gold ions into stable, fluorescent clusters (BSA-AuNCs) [20]. These protein-protected clusters exhibit red fluorescence, excellent water solubility, and low toxicity [21]. However, ultra-small AuNCs face a significant pharmacokinetic hurdle: their size is below the renal filtration threshold (~5.5 nm), leading to rapid clearance from the bloodstream and insufficient tumor accumulation time for effective therapeutic delivery [22]. Recent studies and reviews discussing nanocarrier targeting strategies in solid tumors further underscore that integrating ultrasmall functional nanocomponents into a larger carrier arte to prolong circulation, increase tumor residence time, and enable measurable intracellular delivery outcomes [23].

Consequently, to harness the imaging potential of AuNCs while ensuring effective drug delivery, they must be integrated into a larger, supramolecular carrier system. Chitosan-based matrices have been explored to stabilizet gold nanoclusters, primarily to improve optical robustness and enable sensing/imaging readouts (e.g., chitosan-stabilized AuNC assemblies) or to enhance signal performance via polymer confinement effects (e.g., AuNCs embedded in chitosan nanogels) [24,25]. In contrast, the innovation of the present work is the engineering integration of intrinsically fluorescent, protein-stabilized BSA–AuNCs into a chitosan hybrid nanocarrier designed for chemotherapy delivery, where (i) the carrier architecture is optimized for DOX retention at physiological pH and release under endo/lysosomal acidification, and (ii) the benefit is validated using quantitative gastric-cancer cell outcomes (uptake by flow cytometry/confocal imaging, apoptosis, and IC_{50} shift). This positioning differentiates our platform from prior chitosan–AuNC systems that emphasize fluorescence stabilization/confinement but do not combine a BSA–AuNC trackable core with a pH-gated DOX-transport objective and gastric-cancer cellular validation [26].

Polymeric nanoparticles offer a versatile platform for such integration. Chitosan (CS), a cationic linear polysaccharide derived from the deacetylation of chitin,

10.57647/jnsc.2026.1603.13

stands out as a matrix material due to its biodegradability, mucoadhesiveness, and favorable safety profile [11]. A critical attribute of chitosan is its pH-responsiveness. The amino groups (-NH_2) on the chitosan backbone have a pKa of approximately 6.5 [27].

In the acidic microenvironment of solid tumors (pH 6.5–6.8) and within intracellular endosomes/lysosomes (pH 5.0–5.5), these groups become protonated (-NH_3^+), leading to electrostatic repulsion between polymer chains and subsequent swelling or disassembly of the nanoparticle matrix [28]. This physicochemical trigger can be exploited to engineer "smart" nanocarriers that retain their payload during circulation at physiological pH (7.4) but release it rapidly upon internalization by cancer cells [29].

This research proposes the engineering of a hybrid core-shell nanocarrier system, denoted as CS-BSA-AuNCs@DOX, designed to synergize the diagnostic imaging capabilities of gold nanoclusters with the therapeutic precision of a pH-responsive polymeric delivery vehicle. We hypothesize that encapsulating DOX and BSA-AuNCs within a crosslinked chitosan matrix will protect the drug from premature degradation, prevent rapid renal clearance of the nanoclusters, and facilitate targeted intracellular release in gastric cancer cells. The primary objectives of this study are fourfold.

First, to optimize the synthesis of highly fluorescent BSA-AuNCs and their subsequent encapsulation into chitosan nanoparticles via ionic gelation with sodium tripolyphosphate (TPP).

Second, to conduct an exhaustive physicochemical characterization of the hybrid system using advanced analytical techniques including FTIR, XRD, XPS, TEM, SEM, and BET surface area analysis, thereby elucidating the molecular architecture and interactions within the nanocomposite.

Third, to evaluate the drug loading capacity and pH-dependent release kinetics of the system, employing mathematical modeling to interpret the transport mechanisms.

Fourth, to rigorously validate the biological performance of the nanocarriers against human gastric cancer cell lines (MGC-803 and SGC-7901) in terms of cytotoxicity, cellular uptake efficiency, and hemocompatibility. Importantly, this design provides an explicit multimodal theranostic function: the BSA-AuNC component supplies intrinsic fluorescence for real-time tracing of nanocarrier internalization and intracellular trafficking, while the chitosan network undergoes acid-enhanced protonation and swelling in endo/lysosomal environments to promote pH-responsive DOX release. This work aims to provide a comprehensive mechanistic understanding of how such hybrid nanostructures can be tailored to overcome the limitations of conventional chemotherapy in gastric oncology.

2. Materials and Methods

2.1. Materials

Chloroauric acid ($HAuCl_4 \cdot 3H_2O$), bovine serum albumin (BSA, fraction V), and Chitosan (low molecular weight, deacetylation degree ≥ 75%) were purchased from Sigma-Aldrich (St. Louis, MO, USA). Doxorubicin hydrochloride (DOX·HCl) was obtained from Dalian Meilun Biotechnology Co., Ltd. (Dalian, China). Sodium tripolyphosphate (TPP) and sodium hydroxide (NaOH) were purchased from Sinopharm Chemical Reagent Co., Ltd. (Shanghai, China). Fetal bovine serum (FBS), Dulbecco's modified Eagle's medium (DMEM), penicillin-streptomycin, and trypsin-EDTA were acquired from Gibco (Thermo Fisher Scientific, Waltham, MA, USA). The Cell Counting Kit-8 (CCK-8) was purchased from Beyotime Institute of Biotechnology (Shanghai, China), and the Annexin V-FITC/PI apoptosis detection kit was obtained from BD Biosciences (San Jose, CA, USA). All other chemicals were of analytical grade and used as received.

2.2. Synthesis of BSA-Templated Gold Nanoclusters (BSA-AuNCs)

The synthesis of red-emitting BSA-AuNCs was performed utilizing a biomimetic "one-pot" strategy where BSA served dual roles as a macromolecular template and a reductant [30,31]. In a typical procedure, 5 mL of an aqueous BSA solution (50 mg/mL) was introduced into a 50 mL round-bottom flask thermostated at 37°C. To this, 5 mL of an aqueous $HAuCl_4$ solution (10 mM) was added dropwise under vigorous magnetic stirring (1000 rpm). The mixture was allowed to react for 5 minutes, during which the color transitioned from light yellow to a turbid deep brown, indicating the sequestration of Au^{3+} ions by the protein.

Subsequently, the pH of the reaction mixture was adjusted to approximately 12 by the precise addition of 0.5 mL of NaOH solution (1 M). This alkaline environment is critical to activate the phenolic group of tyrosine residues and the thiol groups of cysteine, facilitating the reduction of Au^{3+} to form the nanoclusters [32]. Formation of BSA-AuNCs was initially indicated by the solution changing to a deep red-brown color and exhibiting red emission under 365 nm UV illumination. To confirm nanocluster formation spectroscopically, UV–visible absorption spectra were collected using a quartz cuvette (1 cm pathlength) over 200–800 nm with deionized water as the blank. Consistent with protein-templated Au nanoclusters, the spectrum showed the dominant BSA band near 280 nm and lacked the ~520 nm surface plasmon resonance band characteristic of larger plasmonic Au nanoparticles, supporting the formation of sub-3 nm, quantum-confined

10.57647/jnsc.2026.1603.13

Au species. Fluorescence spectra were recorded to verify the red emission of BSA-AuNCs (excitation set near the UV maximum, emission collected in the visible–NIR region) as commonly reported for BSA-stabilized AuNCs. The crude product was purified by dialysis (Spectra/Por, MWCO 3.5 kDa) against deionized water for 24 h (water replaced every 4 h) to remove excess alkali and unreacted ions, and the purified solution was stored at 4°C in the dark for subsequent encapsulation experiments.

2.3 Preparation of Hybrid Nanocarriers (CS-BSA-AuNCs@DOX)

The hybrid nanocarriers were fabricated using an optimized ionic gelation method [33][34].

Preparation of Chitosan Solution: Chitosan was dissolved in 1% (v/v) acetic acid solution to a concentration of 2.0 mg/mL and stirred overnight to ensure complete dissolution. The pH of the chitosan solution was then adjusted to 5.0 using 1 M NaOH to ensure the amino groups were protonated but avoiding precipitation (which occurs at pH > 6.0). The solution was filtered through a 0.45 μm membrane to remove any insoluble aggregates.

Nanoparticle Formation: A solution of DOX was prepared by dissolving 2.0 mg of DOX·HCl in 1 mL of ultrapure water [26]. This was mixed with 2 mL of the purified BSA-AuNCs solution (protein concentration of the BSA-AuNCs stock: XX mg/mL, BSA-equivalent; determined by a Micro BCA assay, n = 3, mean ± SD). This combined payload solution was then added to 10 mL of the Chitosan solution (2 mg/mL) and stirred for 30 minutes to allow for the electrostatic equilibration between the cationic chitosan/DOX and the anionic BSA-AuNCs.

Crosslinking was initiated by the dropwise addition of 4 mL of TPP aqueous solution (1.0 mg/mL) into the reaction mixture under high-speed magnetic stirring (1200 rpm) at room temperature using a syringe pump (flow rate 0.5 mL/min). The solution immediately developed a distinct opalescence (Tyndall effect), signifying the formation of nanoparticles via ionic crosslinking between the polycationic chitosan chains and the polyanionic TPP/BSA species. The suspension was stirred for an additional 45 minutes to harden the particles.

Formulation screening and optimization: To generate the optimization data reported in Table 1, we prepared a short formulation series by varying the CS:TPP mass ratio (3:1, 4:1, 5:1, and 6:1; formulations F1–F4) while keeping the chitosan concentration fixed at 2.0 mg/mL and the TPP stock concentration fixed at 1.0 mg/mL. Each formulation was produced using the same mixing order, stirring conditions, and TPP addition rate described below. After particle formation and hardening, aliquots were withdrawn for hydrodynamic size, PDI, and ζ-potential measurements. The 'optimal' formulation was selected based on the combined criteria of (i) absence of visible aggregation, (ii) mean hydrodynamic diameter in the ~100–200 nm range, (iii) low dispersity (PDI < 0.30), and (iv) sufficiently high absolute ζ-potential magnitude (|ζ| ≥ 25–30 mV) to support colloidal stability, and this optimized condition was used for all subsequent drug loading, release, and biological studies.

Purification: The nanoparticle suspension was centrifuged at 14,000 (18,000 ×g) for 30 minutes at 4°C. The supernatant was carefully decanted and retained for the determination of drug encapsulation efficiency. The pellet was washed three times with ultrapure water to remove unreacted reagents and then redispersed in water. For solid-state characterization, the pellet was lyophilized (Freeze Dryer, Christ Alpha 1-2 LDplus) for 48 h. Blank nanocarriers (CS-BSA-AuNCs) were prepared using an identical protocol but omitting the addition of DOX.

2.4 Drug Loading and In Vitro Release Assays

2.4.1 *Determination of Encapsulation Efficiency and Loading Capacity*

The amount of entrapped DOX was determined by the indirect method. The supernatant collected after centrifugation was analyzed for free DOX concentration using UV-vis spectrophotometry at λ_{max} = 480 nm [35,36]. A calibration curve was constructed using standard DOX solutions ranging from 1 to 50 μg/mL ($R^2 > 0.999$) [37]. The Encapsulation Efficiency (EE%) and Drug Loading Capacity (LC%) were calculated using the following equations [38]:

$$EE(\%) = \frac{W_{\text{total}} - W_{\text{free}}}{W_{\text{total}}} \times 100$$

$$LC(\%) = \frac{W_{total} - W_{\text{free}}}{W_{NP}} \times 100$$

Where W_{total} is the total weight of DOX added, W_{free} is the weight of free DOX in the supernatant, and W_{NP} is the total weight of the recovered nanoparticles.

2.4.2. *In Vitro Drug Release Study*

The pH-dependent release of DOX was evaluated using the dialysis bag diffusion technique [39]. Nanoparticles (equivalent to 0.5 mg of DOX) were resuspended in 2 mL of the release medium and transferred into dialysis bags (MWCO 12 kDa). The bags were immersed in 20 mL of PBS adjusted to two distinct pH values: pH 7.4 (simulating physiological blood pH) and pH 5.0 (simulating the acidic endosomal/lysosomal environment) [40]. The release systems were placed in a shaking incubator at 37 ± 0.5°C and 100 rpm. At predetermined time intervals (0.5, 1, 2, 4, 8, 12, 24, 36, 48, 60, 72 h), 1

10.57647/jnsc.2026.1603.13

mL of the release medium was withdrawn and immediately replaced with an equal volume of fresh, pre-warmed medium to maintain sink conditions. The concentration of released DOX was determined spectrophotometrically [41].

2.5. Biological Evaluation

2.5.1. *Cell Culture*

Human gastric cancer cell lines MGC-803 (mucinous gastric carcinoma) and SGC-7901 (metastatic gastric carcinoma) were obtained from the Cell Bank of the Chinese Academy of Sciences (Shanghai, China). Cells were cultured in DMEM supplemented with 10% FBS, 100 U/mL penicillin, and 100 µg/mL streptomycin. Cultures were maintained in a humidified atmosphere containing 5% CO_2 at 37°C. The medium was changed every 2 days, and cells were passaged upon reaching 80-90% confluence.

2.5.2. *Hemocompatibility Assay*

To evaluate the safety of the nanocarriers for intravenous administration, a hemolysis assay was conducted [42]. Fresh blood (2 mL) was collected from a healthy volunteer in heparinized tubes. Red blood cells (RBCs) were isolated by centrifugation at 1500 rpm for 10 minutes and washed three times with sterile PBS until the supernatant was clear. A 2% (v/v) RBC suspension was prepared in PBS. Test samples (CS-BSA-AuNCs@DOX) were diluted in PBS to concentrations of 100, 200, 400, 800, and 1000 µg/mL. 0.5 mL of the RBC suspension was mixed with 0.5 mL of the nanoparticle dispersion. PBS and distilled water were used as negative (0% hemolysis) and positive (100% hemolysis) controls, respectively. The mixtures were incubated at 37°C for 3 h, then centrifuged at 3000 rpm for 10 minutes. The absorbance of the supernatant (hemoglobin) was measured at 540 nm. The hemolysis percentage was calculated as [43]:

$$\text{Hemolysis}(\%) = \frac{A_{\text{sample}} - A_{\text{negative}}}{A_{\text{positive}} - A_{\text{negative}}} \times 100$$

2.5.3. *In Vitro Cytotoxicity Assay*

The cytotoxicity was assessed using the CCK-8 assay [44]. MGC-803 and SGC-7901 cells were seeded into 96-well plates at a density of 5×10^3 cells per well and incubated for 24 h. The culture medium was then removed and replaced with 100 µL of fresh medium containing serial dilutions of free DOX, blank CS-BSA-AuNCs, or CS-BSA-AuNCs@DOX (equivalent DOX concentrations: 0.1, 0.5, 1, 2, 5, 10 µg/mL). After 24 and 48 h of incubation, 10 µL of CCK-8 reagent was added to each well, and the plates were incubated for an additional 2 h. The absorbance was measured at 450 nm using a microplate reader (Bio-Rad). Cell viability was expressed as a percentage of the untreated control. The half-maximal inhibitory concentration (IC_{50}) was calculated using GraphPad Prism software via non-linear regression analysis [45].

2.5.4. *Cellular Uptake and Intracellular Imaging*

Confocal Microscopy: MGC-803 cells were seeded on sterile glass coverslips in 6-well plates (2×10^5 cells/well) and incubated overnight. Cells were treated with free DOX or CS-BSA-AuNCs@DOX (5 µg/mL DOX eq.) for 1 h and 4 h. Subsequently, cells were washed three times with cold PBS, fixed with 4% paraformaldehyde for 15 minutes, and stained with DAPI for 10 minutes to visualize nuclei. Coverslips were mounted on slides and imaged using a Leica TCS SP8 Confocal Laser Scanning Microscope. DOX was excited at 488 nm (emission 560-590 nm), BSA-AuNCs at 405 nm (emission 600-650 nm), and DAPI at 405 nm (emission 440-470 nm) [46–48].

Flow Cytometry: To quantify uptake, MGC-803 cells were seeded in 6-well plates and treated as described above. At predetermined time points, cells were trypsinized, washed twice with cold PBS, and resuspended in 0.5 mL PBS. Fluorescence intensity was analyzed using a BD FACSCalibur flow cytometer (Ex 488 nm/Em 575 nm for DOX), collecting 10,000 events per sample [49].

To minimize spectral cross-talk, uptake quantification was performed exclusively in the DOX detection channel (Ex 488 nm/Em 575 nm). In addition, cells treated with blank CS-BSA-AuNCs (without DOX) were analyzed under identical settings as a background control, confirming that BSA-AuNCs contributed only a near-baseline signal in the DOX channel under these acquisition conditions.

2.5.5. *Apoptosis Analysis*

Apoptosis was detected using the Annexin V-FITC/PI double staining kit [50]. MGC-803 cells were treated with free DOX or nanocarriers (1 µg/mL DOX eq.) for 24 h. Cells were harvested, washed with PBS, and resuspended in binding buffer. 5 µL of Annexin V-FITC and 5 µL of Propidium Iodide (PI) were added, and the suspension was incubated for 15 minutes in the dark at room temperature. The apoptotic profile was analyzed by flow cytometry within 1 h.

2.6. Physicochemical Characterization

Hydrodynamic size, dispersity, and surface charge:

The mean hydrodynamic diameter and polydispersity

10.57647/jnsc.2026.1603.13

index (PDI) of freshly prepard by dynamic light scattering at 25°C after appropriate dilution in ultrapure water to avoid multiple scattering. ζ-Potential was measured by electrophoretic light scattering using the same instrument platform, and values are reported as mean ± SD from independent preparations, consistent with standard DLS/ELS reporting conventions for z-average and PDI derived from cumulant analysis.

UV–visible and fluorescence spectroscopy: UV–visible absorption spectra of BSA-AuNCs, free DOX, and nanoparticle dispersions were recorded in quartz cuvettes (1 cm pathlength) over 200–800 nm.

Fluorescence spectra were acquired to confirm the red emission of BSA-AuNCs and to evaluate emission retention after encapsulation, following typical characterization of protein-stabilized Au nanoclusters.

Electron microscopy: For TEM, diluted samples were drop-cast onto carbon-coated copper grids, allowed to adsorb, and negatively stained with phosphotungstic acid when imaging the polymeric nanoparticles. For SEM, lyophilized powders were mounted on conductive stubs and sputter-coated prior to imaging.

FTIR and XRD: FTIR spectra were recorded for chitosan, BSA-AuNCs, free DOX, and lyophilized nanoparticles to identify characteristic functional groups and interaction-induced shifts.

Powder XRD patterns were collected for the same solid samples over a conventional 2θ range to evaluate DOX crystallinity loss upon encapsulation and to assess whether detectable fcc Au reflections were present (not expected for ultrasmall clusters).

Textural analysis (N_2 adsorption–desorption): The specific surface area and pore parameters of lyophilized nanoparticles were measured by nitrogen adsorption–desorption using Brunauer–Emmett–Teller (BET) analysis for surface area and Barrett–Joyner–Halenda (BJH) analysis for pore size distribution after vacuum degassing.

Thermogravimetric analysis: Thermal stability and inorganic residue content were evaluated by TGA under an inert atmosphere with controlled heating, and residual mass at high temperature was used to support the composite nature of the formulation.

3. Results and Discussion

3.1. Synthesis and Optimization of Nanocarriers

The fabrication of the CS-BSA-AuNCs@DOX system was based on a sequential assembly process involving the biomineralization of gold clusters followed by their encapsulation within a polymeric network. The synthesis of the core BSA-AuNCs was confirmed by a striking color change of the reaction mixture from pale yellow to deep brown upon the addition of NaOH. This transformation is indicative of the reduction of Au^{3+} ions by the tyrosine residues of BSA at alkaline pH (~12), a process well-documented in protein-templated synthesis [20]. Under UV illumination (365 nm), the purified solution exhibited a strong, stable red fluorescence, contrasting sharply with the non-fluorescent nature of the initial gold salt or larger plasmonic gold nanoparticles. This fluorescence arises from the molecule-like electronic transitions of the Au_{25} clusters stabilized within the protein scaffold [51]. The stability of these clusters over several months at 4°C suggests robust protection by the BSA template, likely through multiple Au-S bonds with the 35 cysteine residues present in the protein structure [52]. The encapsulation efficiency and particle characteristics of the hybrid system are critically dependent on the mass ratio of Chitosan (CS) to TPP. We conducted an optimization study varying the CS:TPP mass ratio from 3:1 to 6:1 (**Table 1**).

The results indicate that formulation F3 (5:1 ratio) provided the optimal balance between size, polydispersity, and surface charge. To elucidate the specific role of TPP versus BSA-AuNCs in the crosslinking network, a control experiment was conducted in the absence of TPP. The binary mixture of Chitosan and BSA-AuNCs resulted in a turbid suspension comprising large, unstable aggregates (mean diameter > 450 nm, PDI > 0.6), confirming that while the anionic BSA-AuNCs participate in electrostatic association (acting as a macromolecular co-crosslinker), they lack the charge density and small steric profile required to condense the polymer chains into compact nanospheres. Consequently, TPP is essential to function as the primary 'locking' agent for ionic gelation. At lower ratios (F1, 3:1), the excess of anionic TPP neutralized the cationic charges of chitosan too rapidly, leading to extensive inter-particle bridging and aggregation, evidenced by the large size (210 nm) and high PDI (0.45). The lower zeta potential (+18.5 mV) confirms the high degree of charge neutralization. At higher ratios (F4, 6:1), the insufficient amount of crosslinker resulted in loose, smaller networks with a significantly reduced production yield of 36.1 ± 3.2%, as a substantial fraction of chitosan chains remained un-crosslinked in the supernatant and were removed during the purification process. In contrast, the optimized Formulation F3 achieved a yield of 68.4 ± 2.5%, successfully forming compact, spherical particles with a hydrodynamic diameter of 145 nm and a narrow PDI of 0.18. The zeta potential of +32.4 mV is highly favorable, as magnitudes greater than 30 mV generally ensure colloidal stability through electrostatic repulsion [53]. Moreover, a cationic surface can promote electrostatic association with the negatively charged glycocalyx/cell membrane and is frequently associated with enhanced nanoparticle internalization. However, the specific endocytic route cannot be concluded from surface charge alone.

10.57647/jnsc.2026.1603.13

Table 1. Optimization of formulation parameters (CS concentration fixed at 2 mg/mL)

Formulation Code	CS:TPP Ratio (w/w)	Mean Particle Size (nm)	PDI	Zeta Potential (mV)	Yield (%)	Visual Appearance
F1	3:1	210 ± 12	0.45 ± 0.05	+18.5 ± 2.1	78.2 ± 4.1	Aggregated, turbid
F2	4:1	165 ± 8	0.28 ± 0.03	+26.3 ± 1.4	54.7 ± 3.6	Slightly opalescent
F3	5:1	145 ± 5	0.18 ± 0.02	+32.4 ± 1.2	68.4 ± 2.5	Opalescent (Tyndall effect)
F4	6:1	130 ± 6	0.35 ± 0.04	+38.1 ± 1.8	36.1 ± 3.2	Clear, low yield

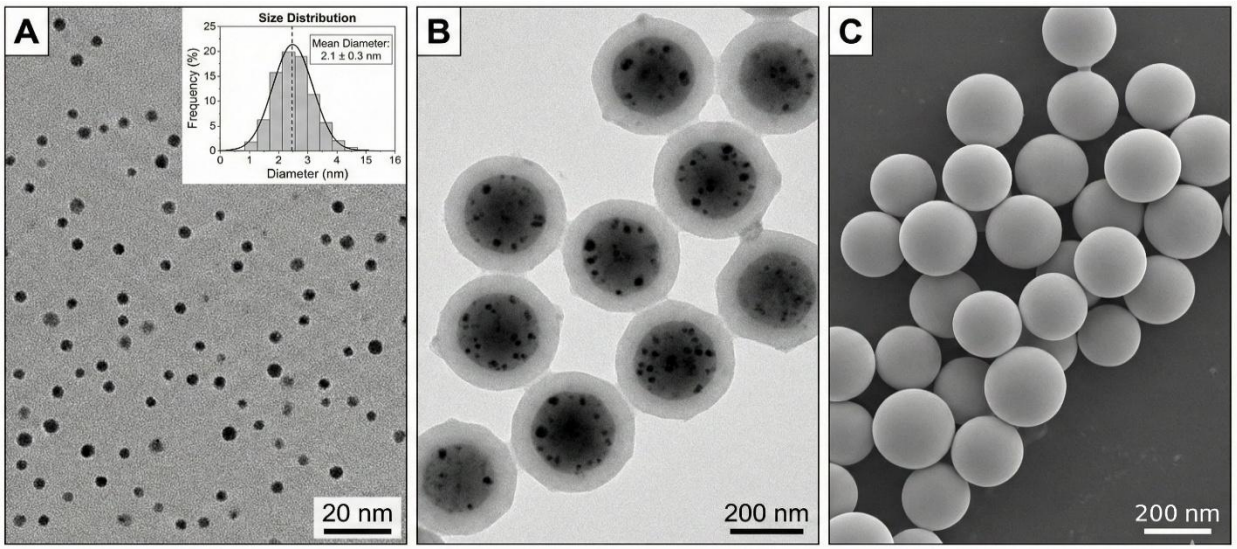

Figure 1. TEM/SEM characterization of BSA-AuNCs and CS-BSA-AuNCs@DOX hybrid nanocarriers**.** (A) TEM image of discrete BSA-AuNCs showing ultra-small, high-contrast dots. (B) TEM image of CS-BSA-AuNCs@DOX nanoparticles after phosphotungstic acid staining, showing a spherical architecture with a lighter polymeric shell/halo and an electron-dense core containing distributed AuNCs. (C) SEM image of the lyophilized CS-BSA-AuNCs@DOX powder showing spherical particles with relatively smooth surfaces

Therefore, we describe the uptake mechanism as a plausible, charge-assisted endocytic process and (where feasible) propose validation using standard endocytosis inhibition assays (e.g., chlorpromazine for clathrin-mediated endocytosis, methyl-β-cyclodextrin/filipin for lipid-raft/caveolae-associated uptake, and amiloride or EIPA for macropinocytosis), interpreted with appropriate controls and awareness of inhibitor limitations[54].

3.2. Physicochemical Characterization

Transmission electron microscopy (TEM) provided direct, morphology-level evidence for the successful construction of the hybrid system. As shown in Fig. 1A, the BSA-templated gold nanoclusters (BSA-AuNCs) were observed as discrete, ultra-small, high-contrast dark dots with an average diameter of 2.1 ± 0.3 nm. No recognizable lattice fringes were detected under the applied imaging conditions, which is consistent with the amorphous/sub-crystalline character typically reported for ultra-small clusters where the atom count is insufficient to sustain a long-range periodic lattice [55].

In contrast, the assembled CS-BSA-AuNCs@DOX nanocarriers exhibited a well-defined spherical morphology in Fig. 1B.

After phosphotungstic acid staining, a lighter polymeric "halo" surrounding a more electron-dense core region was clearly visible, with darker BSA-AuNCs distributed throughout the core domain—collectively confirming effective encapsulation of the clusters within the chitosan network.

The mean particle size measured from TEM micrographs was approximately ~130 nm, slightly smaller than the 145 nm hydrodynamic diameter obtained by DLS, which is plausibly explained by partial collapse/shrinkage of the hydrated polymer shell during the drying step required for TEM sample preparation, whereas DLS reflects the fully hydrated state [56]. Additionally, SEM imaging of the lyophilized product (Fig. 1C) revealed spherical particles with relatively smooth surfaces, supporting the formation of uniform nanostructures rather than irregular aggregates. The optical signatures of each component and the assembled nanocarrier were first evaluated by UV–vis spectroscopy. As shown in Fig. 2A, the BSA-AuNCs spectrum was dominated by the characteristic protein band at 280 nm, while the ~520 nm surface plasmon resonance (SPR) band typically observed for plasmonic Au nanoparticles larger than ~3 nm was absent; instead, a monotonically decaying absorption tail extended into the visible region [57]. This spectral profile supports the formation of quantum-sized Au nanoclusters rather than larger, plasmonic particles.

10.57647/jnsc.2026.1603.13

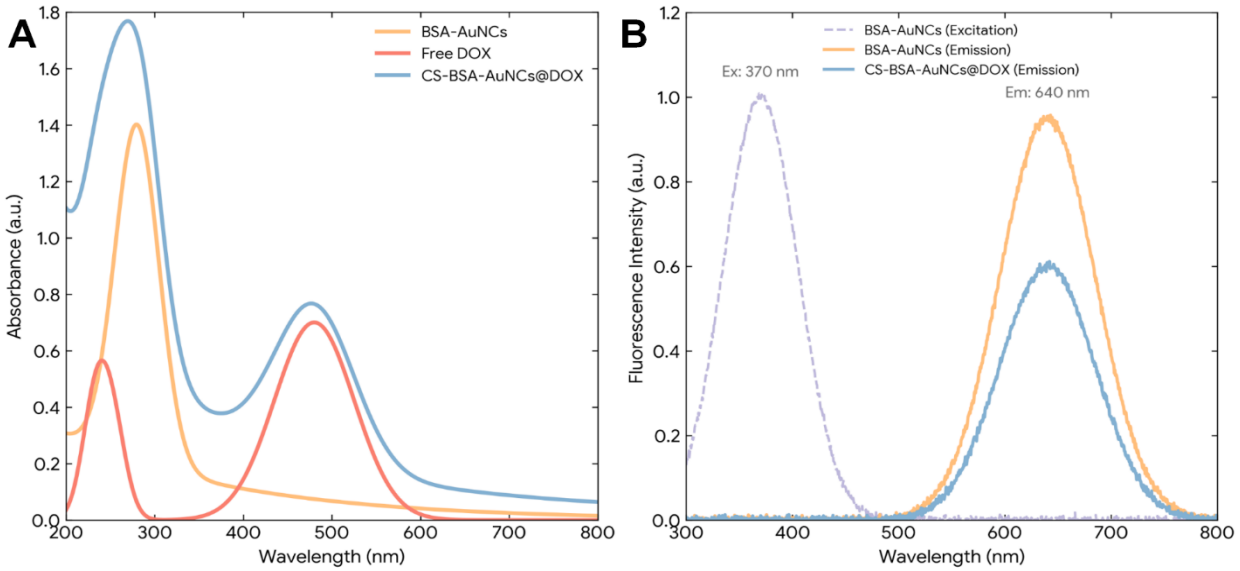

Figure 2. Optical properties and fluorescence behavior of BSA-AuNCs, DOX, and CS-BSA-AuNCs@DOX. (A) UV–vis absorption spectra of BSA-AuNCs, free DOX, and the hybrid nanocarrier. (B) Fluorescence excitation/emission characteristics showing BSA-AuNCs (Ex = 370 nm) with red emission near 640 nm and partial emission quenching after DOX co-loading/encapsulation

Free DOX displayed a broad absorption band centered at ~480 nm, and the CS-BSA-AuNCs@DOX formulation exhibited a superimposed spectrum containing both the strong 280 nm band (BSA) and the DOX-associated absorption around 480 nm, collectively confirming the successful co-loading of AuNCs and DOX within the same carrier (Fig. 2A). Fluorescence spectroscopy further verified the photophysical integrity of the AuNCs after formulation. As shown in Fig. 2B, BSA-AuNCs exhibited an excitation maximum at 370 nm and a strong red emission peak at ~640 nm. After encapsulation and co-loading with DOX, the AuNC emission intensity decreased (partial quenching), which can be reasonably attributed to an inner-filter effect (DOX absorption attenuating emitted photons) and/or Förster resonance energy transfer (FRET) between the AuNC donor and DOX acceptor enabled by spectral overlap and nanoscale proximity within the particle core (Fig. 2B). Because such photophysical coupling can, in principle, influence intensity-based readouts, cellular-uptake quantification was restricted to the DOX channel in flow cytometry, and blank-carrier controls were used to verify negligible AuNC contribution within the DOX detector window under the chosen instrument settings. Importantly, despite the quenching effect, the residual red fluorescence remained sufficiently intense to support intracellular imaging and carrier tracking applications. X-ray diffraction (XRD) was used to resolve the solid-state organization of DOX and the structural ordering of the AuNC-containing systems (Fig. 3A). Pure DOX exhibited multiple sharp, high-intensity reflections (e.g., at 13°, 16°, and 22°), confirming its highly crystalline nature. In contrast, BSA-AuNCs displayed a broad amorphous halo centered around $2\theta \approx 20°$, which is characteristic of proteinaceous matrices, and no discernible fcc Au reflections such as the (111) peak at 38.2° were detected—an expected outcome for sub-2 nm clusters where the coherent scattering domain is too small to yield distinct diffraction maxima. Critically, the characteristic crystalline peaks of DOX disappeared in the CS-BSA-AuNCs@DOX pattern, leaving only the broad halo from the chitosan/BSA framework (Fig. 3A). This indicates that DOX is dispersed predominantly in an amorphous or molecularly mixed state within the polymeric network, which is advantageous for drug delivery because amorphous drugs typically exhibit higher apparent solubility and faster dissolution than their crystalline counterparts [58]. Fourier transform infrared spectroscopy (FTIR) was then used to probe intercomponent interactions governing carrier formation and DOX accommodation (Fig. 3B). Chitosan showed the expected broad O–H/N–H stretching band near 3420 cm^{-1} and an Amide I-related band around 1655 cm^{-1}. For BSA-AuNCs, the Amide I band shifted from 1652 cm^{-1} (pure BSA) to 1648 cm^{-1}, alongside perturbations in the Amide II region (~1540 cm^{-1}), consistent with localized conformational changes and coordination interactions associated with cluster formation. In the hybrid CS-BSA-AuNCs@DOX spectrum, the emergence of a band at 1070 cm^{-1} (assigned to P=O stretching from TPP) supports ionic crosslinking, while the broad ~3400 cm^{-1} envelope shifted to 3405 cm^{-1} and further broadened, indicating strengthened hydrogen bonding and electrostatic association among $–NH_3^+$ (chitosan) and anionic groups (TPP/BSA) [59]. Notably, DOX-related bands (quinone C=O near 1730 cm^{-1} and aromatic skeletal vibrations at 1615 and 1580 cm^{-1}) remained detectable but weakened and slightly shifted, supporting successful incorporation of DOX with matrix-mediated interactions rather than phase-separated crystalline drug domains [60].

10.57647/jnsc.2026.1603.13

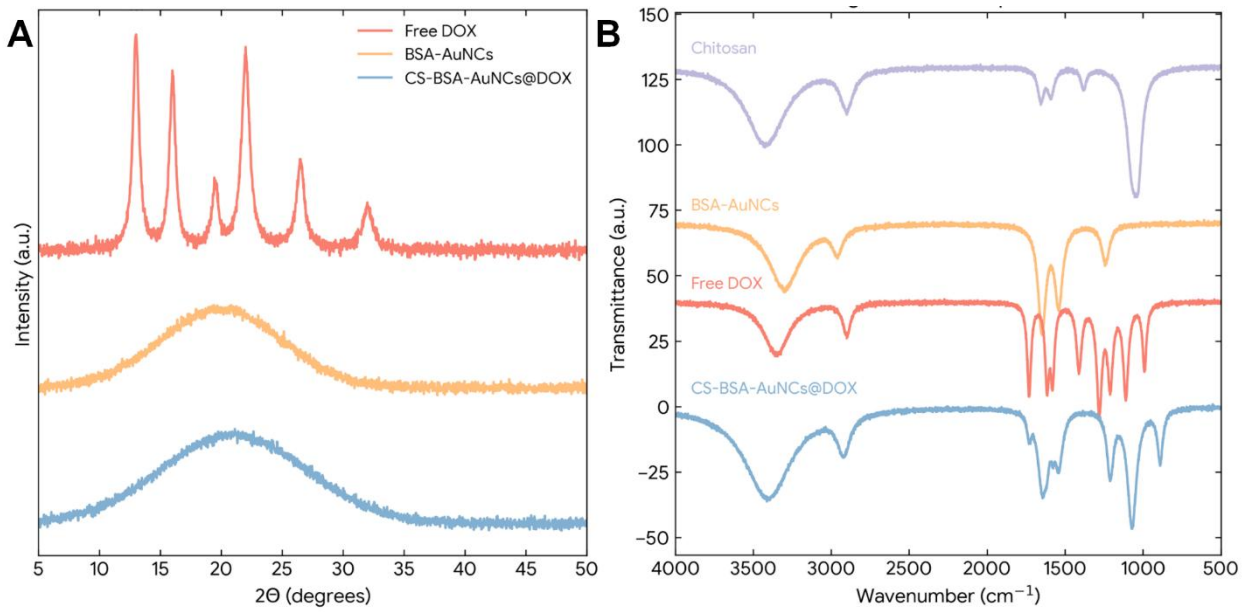

Figure 3. (A) XRD patterns and (B) FTIR spectra of free DOX, BSA-AuNCs, and CS-BSA-AuNCs@DOX by XRD and FTIR

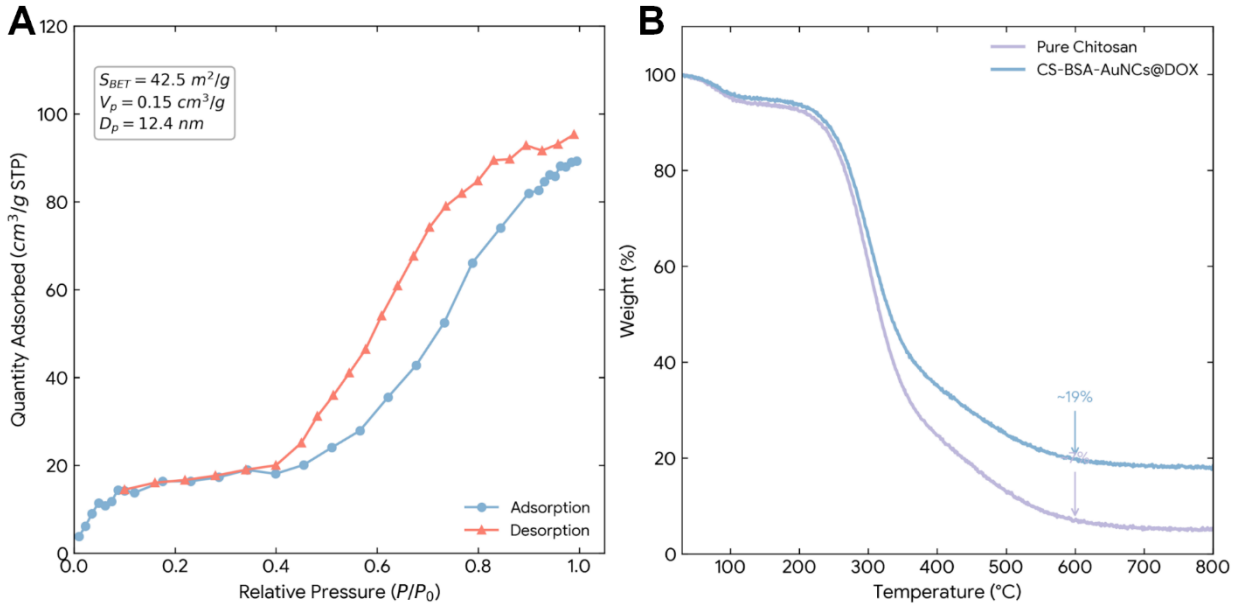

Figure 4. Textural and thermal characterization of CS-BSA-AuNCs@DOX nanocarriers. (A) Nitrogen adsorption–desorption isotherms and corresponding pore characteristics of lyophilized CS-BSA-AuNCs@DOX. (B) TGA curves of pure chitosan and CS-BSA-AuNCs@DOX

Nitrogen adsorption–desorption analysis indicated that the lyophilized CS-BSA-AuNCs@DOX possessed a mesoporous texture suitable for molecular loading and transport (Fig. 4A). The isotherm exhibited a Type IV profile with an H3 hysteresis loop, consistent with mesoporous materials containing slit-like pores typically arising from interparticle aggregation within a polymeric network [61]. Quantitatively, the nanocarriers showed a BET specific surface area (S_{BET}) of 42.5 m^2/g, a total pore volume (V_p) of 0.15 cm^3/g, and an average pore diameter of 12.4 nm (Fig. 4A).

This textural enhancement is notable relative to conventional dried chitosan nanoparticles, which commonly display low surface areas (<10 m^2/g) due to the intrinsically non-porous polymer matrix. Here, the elevated surface area and mesoporosity are most plausibly attributed to the hierarchical organization of BSA-AuNCs within the ionic-gelation framework, generating additional interfacial area and pore pathways. Functionally, these features are advantageous for drug delivery because they increase the accessible surface for DOX association (e.g., hydrogen bonding and hydrophobic interactions) and promote aqueous penetration through the matrix, facilitating diffusion-controlled and hydration-triggered release.

Thermogravimetric analysis further supported the composite nature of the formulation and clarified its thermal stability characteristics (Fig. 4B). Pure chitosan exhibited a dominant decomposition step initiating at approximately 250 °C, consistent with thermal

10.57647/jnsc.2026.1603.13

degradation of the polysaccharide backbone (Fig. 4B). The hybrid CS-BSA-AuNCs@DOX nanocarriers showed a comparable degradation onset, indicating that incorporation of AuNCs and crosslinking chemistry did not markedly lower the initial thermal stability threshold. However, the hybrid material presented a substantially higher residual mass at 600 °C (approximately 18%), compared with ~5% for pure chitosan. The increased char/inorganic residue is attributed to the presence of the inorganic gold component and thermally stable phosphate species associated with TPP crosslinking, providing corroborative evidence that the final product is a true organic–inorganic composite rather than a physically mixed polymer/drug system.

3.3. Drug Loading and Release Kinetics

The optimized formulation (F3) achieved an encapsulation efficiency (EE) of 82.3 ± 1.4% and a drug loading capacity (LC) of 12.6 ± 0.8%, indicating that DOX was incorporated into the nanocarrier with high fidelity. This high EE is best rationalized by a dual retention mechanism, in which DOX is (i) physically confined within the densely crosslinked chitosan/TPP ionic-gel network and (ii) additionally stabilized through electrostatic association with anionic domains contributed by BSA and TPP in the particle interior.

As shown in Fig. 5A, the system exhibited a clear pH-gated ("off–on") release behavior over 72 h. Under physiological conditions (pH 7.4), release was restrained, with only ~22% released at 24 h and a plateau near ~35% by 72 h, supporting structural integrity and reduced premature leakage during circulation.

In contrast, at pH 5.0 (endosomal/lysosomal-like acidity), release accelerated markedly, reaching ~65% by 24 h and ~88% by 72 h (Fig. 6A). Mechanistically, this switch is consistent with enhanced protonation of chitosan amino groups at low pH, which increases charge density and intra/inter-chain repulsion, driving matrix swelling and enlarged mesh size that promote DOX diffusion; concurrently, DOX solubility rises in acidic media due to protonation of its aminosugar, further facilitating outward transport.

To clarify the dominant transport mode under acidic conditions, the pH 5.0 release data were fitted to multipzero-order, first-order, Higuchi, and Korsmeyer–Peppas; Table 2). Among these, the Korsmeyer–Peppas (K–P) model provided the best statistical fit ($R^2 = 0.985$), exceeding the Higuchi ($R^2 = 0.971$) and first-order ($R^2 = 0.945$) fits (Table 2).

For K–P fitting, the initial portion of the profile ($Mt/M\infty \leq 0.60$) was used to minimize late-time deviations commonly observed in swelling/eroding systems. The fitted exponent n = 0.65 (spherical matrix) lies between the Fickian benchmark (n = 0.43) and Case II transport (n = 0.85), indicating anomalous (non-Fickian) release governed by coupled DOX diffusion and acid-enhanced chitosan network relaxation/swelling, consistent with the proposed endo/lysosomal-acidity–triggered deployment mechanism [62] (Table 2; Fig. 5B). The release exponent was n = 0.65, which (for spherical matrices) falls between the Fickian benchmark (n = 0.43) and Case II transport (n = 0.85), indicating anomalous (non-Fickian) transport governed by coupled drug diffusion + polymer relaxation/swelling. This kinetic outcome is consistent with the proposed pH-triggered swelling mechanism and supports endo/lysosomal-acidity–activated intracellular drug deployment.

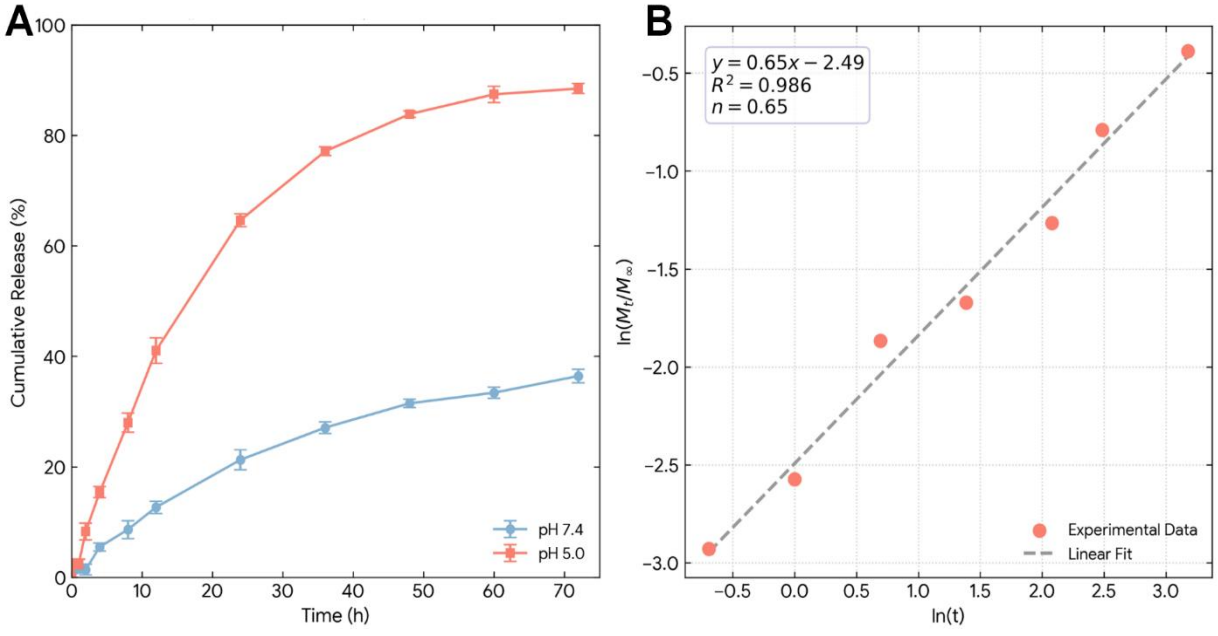

Figure 5. pH-responsive DOX releasef CS-BSA-AuNCs@DOX. (A) Cumulative DOX release profiles over 72 h at pH 7.4 and pH 5.0 (mean ± SD, n = [insert your n] independent release experiments). (B) Linearized Korsmeyer–Peppas fitting plot generated from the mean release values

10.57647/jnsc.2026.1603.13

Table 2. Kinetic release parameters for DOX from CS-BSA-AuNCs@DOX at pH 5.0

Kinetic Model	Mathematical Equation	R^2	Key Parameters	Analysis
Zero-order	$Qt = K_0 t$	0.912	$K_0 = 3.21$ % h^{-1}	Poor correlation, indicating that DOX release does not follow a constant rate independent of concentration.
First-order	$\ln(100 - Qt) = K_1 t$	0.945	$K_1 = 0.083$ h^{-1}	Moderate fit, suggesting partial concentration-dependent release behavior.
Higuchi	$Qt = K_H t^{1/2}$	0.971	$K_H = 18.6$ % $h^{-1/2}$	Good linearity, implying a dominant diffusion-controlled contribution.
Korsmeyer–Peppas	$Mt/M\infty = K t^n$	0.985	$n = 0.65$	Best fit. Linear regression statistically significant ($p < 0.001$). The n value ($0.43 < n < 0.85$) indicates anomalous (non-Fickian) transport, arising from a combination of DOX diffusion and polymer matrix relaxation/swelling under acidic conditions.

3.4. Biological Evaluation

Hemocompatibility is a non-negotiable prerequisite for intravenously administered nanocarriers. As summarized in Fig. 6A, red blood cells (RBCs) exposed to distilled water (positive control) produced a bright red supernatant, whereas PBS (negative control) remained clear; in contrast, CS-BSA-AuNCs@DOX induced negligible hemolysis across the tested concentration range. Quantitatively, hemolysis was 1.2% at 100 μg/mL and remained below 3.0% even at 1000 μg/mL, indicating that the formulation does not measurably compromise RBC membrane integrity under these conditions. Consistent with the commonly used <5% hemolysis criterion for blood-contacting materials, these results support the suitability of the chitosan/BSA-based hybrid architecture for systemic administration [63]. The intrinsic cytocompatibility of the carrier was first confirmed by CCK-8 assays, where blank CS-BSA-AuNCs maintained >90% cell viability even at 500 μg/mL, demonstrating that the vehicle itself is largely non-toxic within the evaluated dose window (Fig. 6B). Under identical conditions, both free DOX and CS-BSA-AuNCs@DOX exhibited dose- and time-dependent growth inhibition in MGC-803 and SGC-7901 gastric cancer cells, but the nanoformulation consistently delivered stronger antiproliferative effects at matched DOX-equivalent concentrations [64]. This enhanced antiproliferative effect is best explained by an increase in the effective intracellular (and nuclear) exposure of DOX delivered by the hybrid carrier rather than a change in the intrinsic pharmacology of DOX.

First, the optimized nanocarriers possess a strongly positive surface potential (+32.4 mV), which can intensify electrostatic association with the negatively charged cell membrane/glycocalyx and thereby increase the probability of endocytic internalization (charge-assisted uptake). Consistent with this delivery advantage, flow cytometry shows markedly higher intracellular DOX signal for CS-BSA-AuNCs@DOX than for free DOX at 4 h (MFI 717 a.u. vs 280 a.u.; ~2.5-fold), demonstrating greater cellular accumulation under identical exposure conditions.

Second, once internalized, the formulation is designed to exploit endo/lysosomal acidity: our release study shows restrained leakage at pH 7.4 (~22% at 24 h; ~35% at 72 h) but substantially accelerated release at pH 5.0 (~65% at 24 h; ~88% at 72 h), which is consistent with protonation-driven chitosan swelling/relaxation and facilitates intracellular DOX liberation after endosomal trafficking. Third, confocal microscopy reveals time-dependent cytoplasmic-to-nuclear redistribution with clear nuclear co-localization by 4 h (Fig. 7B), which is mechanistically relevant because DOX exerts cytotoxicity primarily through nuclear DNA intercalation and topoisomerase II–associated damage. Together, increased uptake plus acid-triggered intracellular release increases the likelihood and magnitude of nuclear DOX exposure, thereby strengthening growth inhibition and lowering the apparent IC_{50}. Similar delivery-driven enhancements are widely reported in the chitosan–DOX nanomedicine literature, including gastric-cancer–relevant models.

The enhanced efficacy is corroborated by the IC_{50} values at 48 h (Table 3), where CS-BSA-AuNCs@DOX reduced the IC_{50} from 1.85 ± 0.12 to 0.92 ± 0.08 μg/mL in MGC-803 cells and from 2.10 ± 0.15 to 1.15 ± 0.10 μg/mL in SGC-7901 cells (≈2.01× and 1.83× potency enhancement, respectively). Mechanistically, this improvement is cdiated uptake process in which the cationic shell enhances initial cell-surface association and thereby increases the likelihood of endocytic internalization relative to free DOX diffusion. Because 'adsorptive endocytosis' remains a hypothesis without pathway-specific validation, we have revised the wording to avoid over-interpretation and outline a standard inhibitor-based verification approach (clathrin-, lipid-raft/caveolae-, and macropinocytosis-associated inhibitors) as a follow-up experiment, interpreted cautiously due to known off-target effects of pharmacological blockers [65].

10.57647/jnsc.2026.1603.13

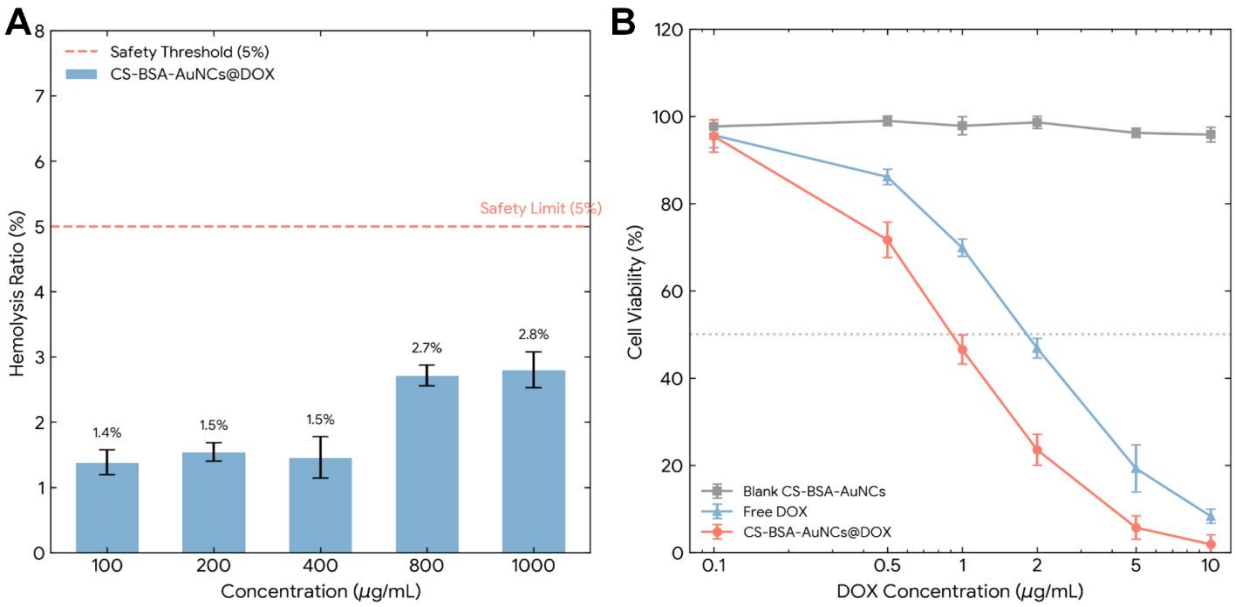

Figure 6. (A) Hemolysis evaluation of CS-BSA-AuNCs@DOX at 100–1000 μg/mL using PBS and distilled water as negative and positive controls, respectively. (B) CCK-8 cell viability profiles of MGC-803 cells treated with blank CS-BSA-AuNCs, free DOX, and CS-BSA-AuNCs@DOX (DOX-equivalent concentrations) for 24 and/or 48 h (mean ± SD, n = 3 independent experiments). Error bars represent SD

Table 3. IC_{50} values (μg/mL) of free DOX and CS-BSA-AuNCs@DOX in MGC-803 and SGC-7901 cells after 48 h incubation, with calculated potency enhancement of the nanocarrier formulation

Cell Line	Free DOX IC_{50}	Nanocarrier IC_{50}	Potency Enhancement
MGC-803	1.85 ± 0.12	0.92 ± 0.08	2.01x
SGC-7901	2.10 ± 0.15	1.15 ± 0.10	1.83x

Flow cytometry provided quantitative confirmation that CS-BSA-AuNCs@DOX markedly enhanced intracellular accumulation in MGC-803 cells (Fig.7A). The cellular fluorescence increased with incubation time, and at 4 h the mean fluorescence intensity (MFI) for the nanocarrier-treated group reached 717 a.u., which was approximately 2.5-fold higher than the free DOX group (280 a.u.) (Fig. 7A). This pronounced uptake advantage is consistent with the presence of a catiotes electrostatic association with the negatively charged glycocalyx/cell membrane, which can increase nanoparticle–cell contact frequency and is often correlated with higher endocytic uptake. Nevertheless, the pathway (e.g., clathrin-mediated, lipid-raft/caveolae-associated, or macropinocytosis) cannot be assigned from these data alone; accordingly, we describe the mechanism as charge-assisted endocytosis and propose confirmation via inhibitor studies (e.g., chlorpromazine, methyl-β-cyclodextrin/filipin, and amiloride/EIPA), ideally combined with low-temperature controls and viability checks to mitigate non-specific effects [54].

Confocal microscopy further resolved the intracellular trafficking behavior and supported successful delivery to the pharmacological target site (Fig. 7B). At 1 h, only weak red fluorescence was detected primarily in the cytoplasm, consistent with early-stage internalization and endosomal localization. By 4 h, the intracellular red signal intensified substantially and showed clear nuclear accumulation, co-localizing with the blue DAPI-stained nuclei, which is critical given that DOX exerts cytotoxicity through DNA intercalation. Importantly, the orange-red fluorescence attributable to BSA-AuNCs remained visible in the cytoplasm during uptake, indicating probe stability under intracellular conditions and enabling real-time optical tracking of the delivery process. This sustained intracellular signal is consistent with the reported high photostability and low photobleaching susceptibility of quantum-confined AuNC emitters (including protein-stabilized clusters), which are frequently highlighted as an advantage over conventional organic dyes for longitudinal fluorescence imaging [57]. From a biosafety perspective, our data show that the blank carriers preserved >90% viability at 500 μg/mL and the formulated nanocarriers induced <3% hemolysis at 1000 μg/mL, supporting in vitro cytocompatibility and hemocompatibility within the tested ranges. These results align with prior reports that BSAhitosan-stabilized/self-assembled AuNCs can exhibit low cytotoxicity and favorable biocompatibility profiles, including feasibility for in vivo imaging/biodistribution studies [66]. Collectively, the combination of persistent AuNC fluorescence for intracellular tracing and a biocompatible polymer/protein hybrid matrix for drug transport supports the theranostic potential of CS-BSA-AuNCs@DOX as a trackable chemotherapy delivery platform [57].

10.57647/jnsc.2026.1603.13

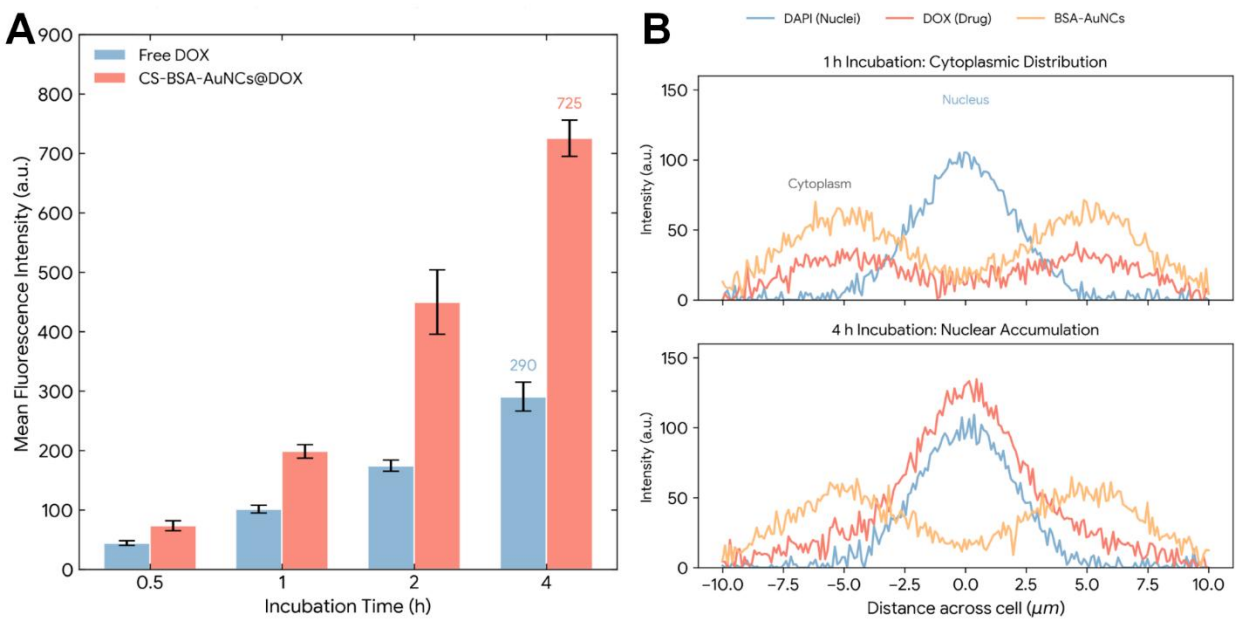

Figure 7. Cellular uptake and intracellular distribution of CS-BSA-AuNCs@DOX in MGC-803 cells. (A) Flow cytometry quantification of cellular uptake over time for free DOX and CS-BSA-AuNCs@DOX (mean ± SD, n = 3 independent experiments). (B) Confocal laser scanning microscopy images after 1 h and 4 h incubation showing DOX fluorescence and nuclei stained with DAPI

To confirm that the growth inhibition induced by CS-BSA-AuNCs@DOX was predominantly mediated through programmed cell death rather than nonspecific membrane damage, MGC-803 cells were analyzed by Annexin V-FITC/PI dual staining followed by flow cytometry.

As shown in Fig. 8A, the untreated control population remained largely viable (94.5% in the Annexin V^-/PI^- quadrant), indicating a low baseline level of spontaneous apoptosis under the assay conditions. Treatment with free DOX produced a pronounced shift toward Annexin V–positive events, yielding a 40.6% total apoptotic fraction (early + late apoptosis), consistent with the canonical mechanism of DOX involving nuclear DNA damage and downstream activation of apoptosis. Notably, CS-BSA-AuNCs@DOX further increased the apoptotic response to 59.0%, demonstrating that the nanocarrier formulation not only preserves DOX bioactivity but also amplifies apoptosis at an equivalent drug exposure window. Importantly, the distribution across apoptotic stages providenanocarrier group exhibited a substantially higher proportion of cells undergoing early apoptosis (Annexin V^+/PI^-) (35.6%) compared with free DOX (22.1%). This enrichment in early apoptotic commitment is most consistent with enhanced nuclear DOX exposure, because DOX exerts its primary cytotoxic action in the nucleus via DNA intercalation and topoisomerase II–mediated DNA damage, which activates DNA-damage signaling and triggers apoptosis [67].

In our study, this causal chain is supported by the uptake/trafficking results: the nanocarrier yields markedly higher intracellular accumulation (Fig. 7A) and shows clear cytoplasmic-to-nuclear redistribution by confocal microscopy (Fig. 7B), where nuclear co-localization becomes evident at 4 h. Enhanced intracellular release under endo/lysosomal acidity is expected to further elevate the effective intracellular concentration and increase the probability of DOX reaching the nucleus, thereby nto early apoptosis while membrane integrity is still preserved (PI exclusion).

Similar relationships—delivery-driven increases in nuclear DOX accumulation accompanied by strengthened apoptotic signaling—have been reported for pH-triggered and endosomal-escape–facilitating DOX delivery systems [68]. A plausible explanation is consistent with the intracellular delivery pathway inferred from the uptake release behavior: the cationic chitosan shell can promote cell-surface association and increase the probability of endocytic internalization, thereby elevating intracellular drug exposure compared with free DOX. Because the precise uptake route has not been experimentally dissected here, we avoid specifying ‘adsorptive endocytosis’ as a confirmed mechanism and instead describe a charge-assisted endocytic hypothesis, with endocytosis-inhibitor studies suggested as a direct validation step [69,70]. Following endosomal trafficking, the acidic endo/lysosomal environment is expected to enhance chitosan protonation and matrix swelling, enabling accelerated DOX liberation and elevating the effective intracellular concentration over time [71]. This localized, acid-triggered release can function as a “lysosome-initiated” amplification step, increasing the probability of downstream nuclear accumulation of DOX and reinforcing DNA damage signaling, which collectively favors early apoptotic initiation and progression [72].

10.57647/jnsc.2026.1603.13

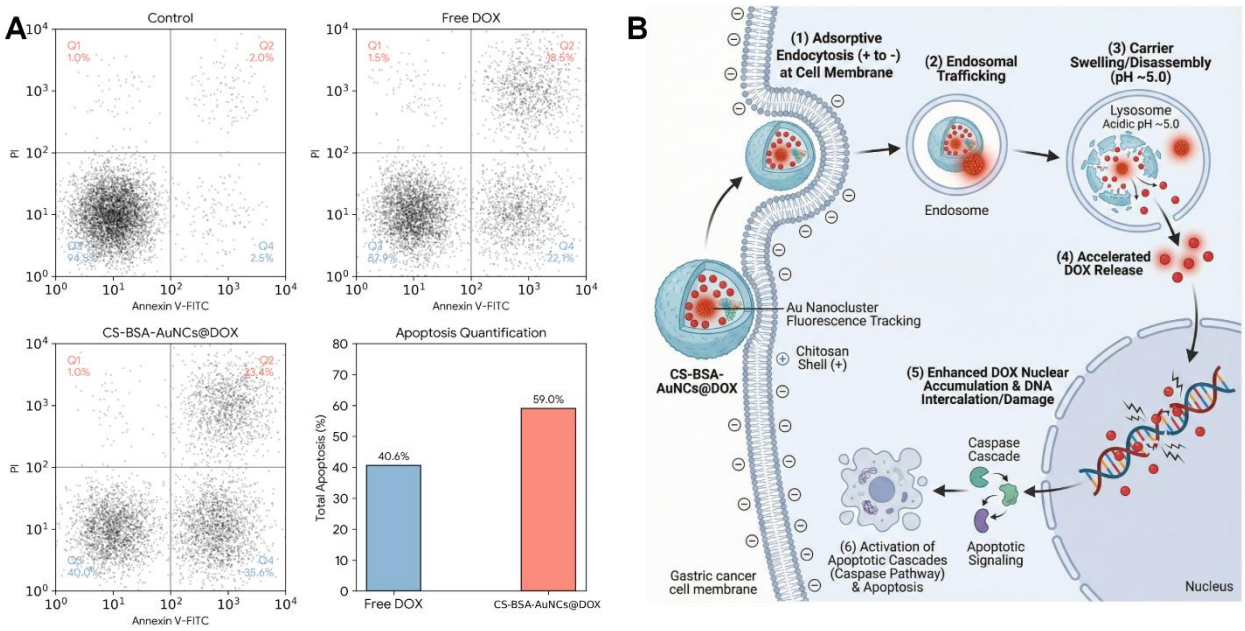

Figure 8. Apoptosis induction by CS-BSA-AuNCs@DOX and the proposed intracellular mechanism. (A) Representative Annexin V-FITC/PI flow-cytometry dot plots of MGC-803 cells after treatment with control, free DOX, or CS-BSA-AuNCs@DOX. (B) Schematic illustration of the apoptosis-amplifying delivery pathway

To make this causal chain explicit and to visually connect the endpoint Annexin V/PI phenotype with upstream intracellular events, a mechanistic schematic is included in Fig. 8B, summarizing the sequence of cationic-shell–mediated internalization, endo/lysosomal trafficking, acid-triggered release, nuclear targeting, and apoptosis activation. Overall, the Annexin V-FITC/PI profiles, together with the proposed intracellular pathway, provide direct evidence that the superior anticancer efficacy of CS-BSA-AuNCs@DOX arises from enhanced apoptosis induction, with a distinct bias toward early apoptotic commitment, rather than from nonspecific cytolysis.

4. Conclusion

In this study, we successfully engineered a novel pH-responsive and fluorescence-traceable hybrid nanocarrier, CS-BSA-AuNCs@DOX, for the enhanced delivery of doxorubicin to gastric cancer cells. By integrating bovine serum albumin–templated gold nanoclusters into an ionically crosslinked chitosan matrix, we developed a core–shell architecture that combines high drug loading capacity with intrinsic optical tracking capabilities. Physicochemical characterization confirmed that the optimized formulation possesses a mesoporous texture and a cationic surface charge (+32.4 mV), features that are critical for drug payload accommodation and cellular interaction. The system demonstrated "smart" drug release behavior, effectively minimizing premature leakage at physiological pH (7.4) while accelerating doxorubicin release under acidic conditions (pH 5.0) typical of the endo/lysosomal microenvironment. Kinetic analysis revealed that this acid-triggered release follows the Korsmeyer–Peppas model, driven by the swelling and relaxation of the chitosan network. Biological evaluations in MGC-803 and SGC-7901 gastric cancer cells demonstrated that the nanocarriers significantly enhanced cellular uptake compared to free doxorubicin, resulting in a roughly two-fold increase in cytotoxicity and a marked reduction in IC50 values. Furthermore, the formulation potentiated the induction of apoptosis, specifically increasing the population of cells in the early apoptotic stage, which correlates with the successful nuclear delivery of the chemotherapeutic agent. Importantly, the blank nanocarriers exhibited excellent cytocompatibility and hemocompatibility, supporting their safety profile for potential systemic administration. Finally, confocal microscopy validated the system's utility as a visually trackable chemotherapy delivery platform, where the stable red fluorescence of the encapsulated AuNCs enabled the real-time monitoring of intracellular trafficking and nuclear accumulation without the need for additional organic dyes. Collectively, these findings present CS-BSA-AuNCs@DOX as a promising candidate for gastric cancer therapy, offering a robust strategy to overcome cellular delivery barriers through environment-responsive transport and integrated optical traceability.

Acknowledgements

This work has been supported by Guangdong Basic and Applied Basic Research Foundation (2022A1515110768), Shenzhen Science and Technology Program (JCYJ20230807110305012), Research Funding after Finishing Postdoctoral Research and Staying

10.57647/jnsc.2026.1603.13

in/Coming to Shenzhen.

Author Contributions

Y.H. conceived the study, defined the research objectives, and supervised the project. J.C. developed the methodology, performed the experiments, conducted the formal data analysis, curated the data, and prepared the original draft of the manuscript. C.-S.W. contributed to data interpretation, visualization, and critical revision of the manuscript. Y.H. acquired funding and oversaw project administration. All authors reviewed and edited the manuscript and have read and agreed to the published version of the manuscript.

Availability of Data and Materials

The data supporting the findings of this study are available from the corresponding author upon reasonable request.

Conflict of Interest

The authors declare that they have no known competing financial interests or personal relationships that could have appeared to influence the work reported in this paper.

Ethical Approval

All procedures involving human blood samples were conducted in accordance with the ethical standards of the institutional research committee and with the Declaration of Helsinki. The hemolysis assay was performed using blood obtained from a healthy volunteer after informed consent. The study protocol was reviewed and approved by the Ethics Committee of The Seventh Affiliated Hospital, Sun Yat-sen University (Approval No.: KY-2025-337-01).

References

[1] Thrift, A. P.; Wenker, T. N.; El-Serag, H. B. Global burden of gastric cancer: epidemiological trends, risk factors, screening and prevention. *Nat Rev Clin Oncol* **20**, 338–349 (2023).

[2] Wang, S.; Li, J.; Zhang, Z.; Cao, S.; Zhang, Z.; Bian, Y.; Xu, Y.; Ma, C. Advances in nanomedicine and delivery systems for gastric cancer research. *Front Bioeng Biotechnol* **13**, 1565999 (2025).

[3] Bisht, A.; Avinash, D.; Sahu, K. K.; Patel, P.; Das Gupta, G.; Kurmi, B. D. A comprehensive review on doxorubicin: mechanisms, toxicity, clinical trials, combination therapies and nanoformulations in breast cancer. *Drug Deliv Transl Res* **15**, 102–133 (2025).

[4] Wu, L.; Meng, Y.; Zheng, X.; Bai, Y.; Han, C.; Wang, Z.; Yang, J.; Jing, X.; Yao, Y. Pillar[5]arene-based prodrug as a GSH-responsive SO_2 nanogenerator for effective gas cancer therapy. *Chin Chem Lett* **36**, 110808 (2025).

[5] Qin, N.; Fan, Y.; Yang, T.; Yang, Z.; Fan, D. The burden of gastric cancer and possible risk factors from 1990 to 2021, and projections until 2035: findings from the Global Burden of Disease Study 2021. *Biomark Res* **13**, 5 (2025).

[6] Go, G.; Lee, C.-S.; Yoon, Y. M.; Lim, J. H.; Kim, T. H.; Lee, S. H. PrPC aptamer-conjugated gold nanoparticles for targeted delivery of doxorubicin to colorectal cancer cells. *Int J Mol Sci* **22**, 1976 (2021).

[7] Rawat, P. S.; Jaiswal, A.; Khurana, A.; Bhatti, J. S.; Navik, U. Doxorubicin-induced cardiotoxicity: an update on the molecular mechanism and novel therapeutic strategies for effective management. *Biomed Pharmacother* **139**, 111708 (2021).

[8] Lin, A.; Giuliano, C. J.; Palladino, A.; John, K. M.; Abramowicz, C.; Yuan, M. L.; Sausville, E. L.; Lukow, D. A.; Liu, L.; Chait, A. R.; *et al.* Off-target toxicity is a common mechanism of action of cancer drugs undergoing clinical trials. *Sci Transl Med* **11**, eaaw8412 (2019).

[9] Dai, Y.; Yu, W.; Cheng, Y.; Zhou, Y.; Zou, J.; Meng, Y.; Chen, F.; Qian, Y.; Yao, Y. Recent developments in pillar[5]arene-based nanomaterials for cancer therapy. *Chem Commun* **61**, 2484–2495 (2025).

[10] Cai, Y.; Zhang, Y.; Liang, X.; Deng, C.; Zhang, J.; Wang, H.; Duan, H.; Yao, Y. A water-soluble cationic [2]biphenyl-extended pillar[6]arene: synthesis, host–guest interaction with hemin and application in chemodynamic/photodynamic cancer therapy. *Chem Commun* **61**, 5333–5336 (2025).

[11] Ashrafizadeh, M.; Hushmandi, K.; Mirzaei, S.; Bokaie, S.; Bigham, A.; Makvandi, P.; Rabiee, N.; Thakur, V. K.; Kumar, A. P.; Sharifi, E.; *et al.* Chitosan-based nanoscale systems for doxorubicin delivery: exploring biomedical application in cancer therapy. *Bioeng Transl Med* **8**, e10325 (2022).

[12] Sharma, A.; Sharma, N.; Singh, S.; Dua, K. Review on theranostic and neuroprotective applications of nanotechnology in multiple sclerosis. *J Drug Deliv Sci Technol* **81**, 104220 (2023).

[13] John, J. Advancements in nano-based drug delivery systems for therapeutics: a comprehensive review. *RSC Pharm* —, — (2025).

[14] Gul, M.; Kashif, M.; Muhammad, S.; Azizi, S.; Sun, H. Various methods of synthesis and applications of gold-based nanomaterials: a detailed review. *Cryst Growth Des* **25**, 2227–2266 (2025).

[15] Jin, R.; Wang, Q.; Dou, G.; Bai, Y.; Liu, S.; Cai, B.; Chen, X. Stimuli-responsive nanoplatform with mitochondria-specific multiple-modal therapeutics for effective tumor treatment. *Appl Mater Today* **21**, 100883 (2020).

[16] Zhang, P.; Hou, H.; Xu, S.; Wen, Y.; Zhang, Y.; Xing, F. Localized surface plasmon resonance sensing based on monometallic gold nanoparticles: from material preparation to detection of bioanalytes. *Anal Methods* **17**, 892–915 (2025).

[17] Waitkus, J.; Chang, Y.; Liu, L.; Puttaswamy, S. V.; Chung, T.; Molina Vargas, A. M.; Dollery, S. J.; O'Connell, M. R.; Cai, H.; Tobin, G. J.; *et al.* Gold nanoparticle-enabled localized surface plasmon resonance on unique gold nanomushroom structures for on-chip CRISPR-Cas13a sensing. *Adv Mater Interfaces* **10**, 2201261 (2023).

[18] Lian, S.; Lamprou, D.; Zhao, M. Electrospinning technologies for the delivery of biopharmaceuticals: current status and future trends. *Int J Pharm* **651**, 123641 (2024).

[19] Wang, T.; Xiao, D. Rapid synthesis of fluorescent bovine serum albumin–gold nanoclusters complex for glutathione determination. *Microchim Acta* **188**, 484 (2021).

[20] Jahanban-Esfahlan, A.; Ostadrahimi, A.; Jahanban-Esfahlan, R.; Roufegarinejad, L.; Tabibiazar, M.;

Amarowicz, R. Recent developments in the detection of bovine serum albumin. *Int J Biol Macromol* **138**, 602–617 (2019).

[21] Hembury, M.; Beztsinna, N.; Asadi, H.; van den Dikkenberg, J. B.; Meeldijk, J. D.; Hennink, W. E.; Vermonden, T. Luminescent gold nanocluster-decorated polymeric hybrid particles with assembly-induced emission. *Biomacromolecules* **19**, 2841–2848 (2018).

[22] Kumari, R.; Sharma, N.; Karwasra, R.; Khanna, K. Colon cancer and their targeting approaches through nanocarriers: a review. *Asian Pac J Trop Biomed* **13**, 104 (2023).

[23] Jin, R.; Liu, Z.; Bai, Y.; Zhou, Y.; Gooding, J. J.; Chen, X. Core–satellite mesoporous silica–gold nanotheranostics for biological stimuli-triggered multimodal cancer therapy. *Adv Funct Mater* **28**, 1801961 (2018).

[24] Lu, J.; Li, Y.; Qin, X.; Wang, Z.; Ouyang, A.; Su, B.; Guo, H.; Yang, X.; Shen, Z.; Li, J.; *et al.* A clinically inspired olsalazine-based metal–organic framework enables a universal nanodrugs platform for diverse disease. *J Colloid Interface Sci* **702**, 138849 (2026).

[25] Duan, Y.; Duan, R.; Liu, R.; Guan, M.; Chen, W.; Ma, J.; Chen, M.; Du, B.; Zhang, Q. Chitosan-stabilized self-assembled fluorescent gold nanoclusters for cell imaging and biodistribution in vivo. *ACS Biomater Sci Eng* **4**, 1055–1063 (2018).

[26] Zare, N.; Karimi-Maleh, H.; Zhang, Z.; Fu, L.; Rouhi, J.; Zhong, N.; Wen, Y.; Ghalkhani, M. Enhancing cancer biomarker identification: precise monitoring of MUC1 using V2C/Au nanocomposite-amplified electrochemical biosensor. *Carbon Lett* **35**, 1691–1700 (2025).

[27] Madhusudhan, A.; Reddy, G. B.; Venkatesham, M.; Veerabhadram, G.; Kumar, D. A.; Natarajan, S.; Yang, M.-Y.; Hu, A.; Singh, S. S. Efficient pH-dependent drug delivery to target cancer cells by gold nanoparticles capped with carboxymethyl chitosan. *Int J Mol Sci* **15**, 8216–8234 (2014).

[28] Imantay, A.; Mashurov, N.; Zhaisanbayeva, B. A.; Mun, E. A. Doxorubicin-conjugated nanoparticles for potential use as drug delivery systems. *Nanomaterials* **15**, 133 (2025).

[29] Xie, J.; Zheng, Y.; Ying, J. Y. Protein-directed synthesis of highly fluorescent gold nanoclusters. *J Am Chem Soc* **131**, 888–889 (2009).

[30] Hsu, N.-Y.; Lin, Y.-W. Microwave-assisted synthesis of bovine serum albumin–gold nanoclusters and their fluorescence-quenched sensing of Hg^{2+} ions. *New J Chem* **40**, 1155–1161 (2016).

[31] Chevrier, D.; Thanthirige, V.; Luo, Z.; Driscoll, S.; Cho, P.; MacDonald, M.; Yao, Q.; Guda, R.; Xie, J.; Johnson, E.; *et al.* Structure and formation of highly luminescent protein-stabilized gold clusters. *Chem Sci* **9**, 2782–2790 (2018).

[32] Calvo, P.; Remuñán-López, C.; Vila-Jato, J. L.; Alonso, M. J. Novel hydrophilic chitosan–polyethylene oxide nanoparticles as protein carriers. *J Appl Polym Sci* **63**, 125–132 (1997).

[33] Gan, Q.; Wang, T.; Cochrane, C.; McCarron, P. Modulation of surface charge, particle size and morphological properties of chitosan–TPP nanoparticles intended for gene delivery. *Colloids Surf B Biointerfaces* **44**, 65–73 (2005).

[34] Al-Shadidi, J. R. M. H.; Al-Shammari, S.; Al-Mutairi, D.; Alkhudhair, D.; Thu, H. E.; Hussain, Z. Chitosan nanoparticles for targeted cancer therapy: a review of stimuli-responsive, passive, and active targeting strategies. *Int J Nanomedicine* **19**, 8373–8400 (2024).

[35] Wang, J., Tian, Q., Liu, Y., et al. Targeting metalloptosis in tumor therapy: from molecular mechanisms to application of metal nanoparticles. *Mol Cancer* **24**, 260 (2025).

[36] Tian, G.; Sun, X.; Bai, J.; Dong, J.; Zhang, B.; Gao, Z.; Wu, J. Doxorubicin-loaded dual-functional hyaluronic acid nanoparticles: preparation, characterization and antitumor efficacy in vitro and in vivo. *Mol Med Rep* **19**, 133–142 (2019).

[37] Zare, M.; Mohammadi Samani, S.; Sobhani, Z. Enhanced intestinal permeation of doxorubicin using chitosan nanoparticles. *Adv Pharm Bull* **8**, 411–417 (2018).

[38] Aziz, A.; Sefidbakht, Y.; Rezaei, S.; Kouchakzadeh, H.; Uskoković, V. Doxorubicin-loaded, pH-sensitive albumin nanoparticles for lung cancer cell targeting. *J Pharm Sci* **111**, 1187–1196 (2022).

[39] Gisbert-Garzarán, M.; Manzano, M.; Vallet-Regí, M. pH-responsive mesoporous silica and carbon nanoparticles for drug delivery. *Bioengineering (Basel)* **4**, 3 (2017).

[40] Dornjak, L.; Kovačić, M.; Ostojić, K.; Angaits, A.; Szpunar, J.; Urlić, I.; Rogina, A. Chitosan–boric acid scaffolds for doxorubicin delivery in osteosarcoma treatment. *Polymers* **14**, 4753 (2022).

[41] de la Harpe, K. M.; Kondiah, P. P. D.; Choonara, Y. E.; Marimuthu, T.; du Toit, L. C.; Pillay, V. The hemocompatibility of nanoparticles: a review of cell–nanoparticle interactions and hemostasis. *Cells* **8**, 1209 (2019).

[42] Yedgar, S.; Barshtein, G.; Gural, A. Hemolytic activity of nanoparticles as a marker of their hemocompatibility. *Micromachines (Basel)* **13**, 2091 (2022).

[43] Xu, J.; Liu, D.; Niu, H.; Zhu, G.; Xu, Y.; Ye, D.; Li, J.; Zhang, Q. Resveratrol reverses doxorubicin resistance by inhibiting epithelial–mesenchymal transition through modulating PTEN/Akt signaling pathway in gastric cancer. *J Exp Clin Cancer Res* **36**, 19 (2017).

[44] He, Y.; Zhu, Q.; Chen, M.; Huang, Q.; Wang, W.; Li, Q.; Huang, Y.; Di, W. The changing 50% inhibitory concentration (IC50) of cisplatin: a pilot study on artifacts of the MTT assay and precise measurement of density-dependent chemoresistance in ovarian cancer. *Oncotarget* **7**, 70803–70821 (2016).

[45] Zhou, J.; Li, K.; Zang, X.; Xie, Y.; Song, J.; Chen, X. ROS-responsive galactosylated nanoparticles with doxorubicin entrapment for triple-negative breast cancer therapy. *Int J Nanomedicine* **18**, 1381–1397 (2023).

[46] Yin, T.; Zhang, Q.; Wu, H.; Gao, G.; Shapter, J. G.; Shen, Y.; He, Q.; Huang, P.; Qi, W.; Cui, D. In vivo high-efficiency targeted photodynamic therapy of ultrasmall Fe_3O_4@polymer nanoprobes based on small-size effect. *NPG Asia Mater* **9**, e383 (2017).

[47] Norouzi, M.; Yathindranath, V.; Thliveris, J. A.; Kopec, B. M.; Siahaan, T. J.; Miller, D. W. Doxorubicin-loaded iron oxide nanoparticles for glioblastoma therapy: a combinational approach for enhanced delivery. *Sci Rep* **10**,

11292 (2020).

[48] Zhang, A.; Pan, S.; Zhang, Y.; Chang, J.; Cheng, J.; Huang, Z.; Li, T.; Zhang, C.; de la Fuente, J. M.; Zhang, Q.; *et al.* Carbon–gold hybrid nanoprobes for real-time imaging, photothermal/photodynamic and nanozyme oxidative therapy. *Theranostics* **9**, 3443–3461 (2019).

[49] Yang, S.; Liang, N.; Li, H.; Xue, W.; Hu, D.; Jin, L.; Zhao, Q.; Yang, S. Design, synthesis and biological evaluation of novel betulinic acid derivatives. *Chem Cent J* **6**, 141 (2012).

[50] Wang, Z.; Su, B.; Ouyang, A.; Liang, Z.; Yuan, P.; Qin, X.; Li, Y.; Huang, X.; Fan, L.; Guo, H.; Jin, R. Reengineering glycyrrhetinic acid into a therapeutic oligomer for targeted tumor therapy with cardioprotection. *J Nanobiotechnol* **23**, 715 (2025).

[51] Weerawardene, K. L. D. M.; Aikens, C. M. Theoretical insights into the origin of photoluminescence of $Au_{25}(SR)_{18}^-$ nanoparticles. *J Am Chem Soc* **138**, 11202–11210 (2016).

[52] Raj, L. F. A. A.; Jonisha, R.; Revathi, B.; Jayalakshmy, E. Preparation and characterization of bovine serum albumin and chitosan nanoparticles for sustainable delivery system of quercetin. *J Appl Pharm Sci* **5**, 001–005 (2015).

[53] Palanikumar, L.; Al-Hosani, S.; Kalmouni, M.; Nguyen, V. P.; Ali, L.; Pasricha, R.; Barrera, F. N.; Magzoub, M. pH-responsive high-stability polymeric nanoparticles for targeted delivery of anticancer therapeutics. *Commun Biol* **3**, 95 (2020).

[54] Wu, J.; Jiang, K.; Wang, X.; Wang, C.; Zhang, C. On–off–on gold nanocluster-based near-infrared fluorescent probe for recognition of Cu(II) and vitamin C. *Microchim Acta* **184**, 1315–1324 (2017).

[55] Zhang, S.; Wang, C. Precise analysis of nanoparticle size distribution in TEM images. *Methods Protoc* **6**, 63 (2023).

[56] van de Looij, S. M.; Hebels, E. R.; Viola, M.; Hembury, M.; Oliveira, S.; Vermonden, T. Gold nanoclusters: imaging, therapy, and theranostic roles in biomedical applications. *Bioconjug Chem* **33**, 4–23 (2022).

[57] Heng, W.; Wei, Y.; Zhou, S.; Ma, D.; Gao, Y.; Zhang, J.; Qian, S. Effects of temperature and ionic strength of dissolution medium on the gelation of amorphous lurasidone hydrochloride. *Pharm Res* **36**, 72 (2019).

[58] Rajabimashhadi, Z.; Masi, A.; Bagheri, S.; Mele, C.; Colangelo, G.; Paladini, F.; Pollini, M. Development and characterization of chitosan microparticles via ionic gelation for drug delivery. *Polymers* **17**, 2603 (2025).

[59] Jin, R.; Xie, J.; Yang, X.; Tian, Y.; Yuan, P.; Bai, Y.; Liu, S.; Cai, B.; Chen, X. A tumor-targeted nanoplatform with stimuli-responsive cascaded activities for multimodal tumor therapy. *Biomater Sci* **8**, 1865–1874 (2020).

[60] Blachnio, M.; Zienkiewicz-Strzałka, M.; Deryło-Marczewska, A. Synthesis of composite sorbents with chitosan and varied silica phases for adsorption of anionic dyes. *Molecules* **29**, 2087 (2024).

[61] Vigata, M.; Meinert, C.; Hutmacher, D. W.; Bock, N. Hydrogels as drug delivery systems: a review of current characterization and evaluation techniques. *Pharmaceutics* **12**, 1188 (2020).

[62] Zhang, B.; Li, Q.; Xu, Q.; Li, B.; Dong, H.; Mou, Y. Polydopamine-modified ceria nanorods alleviate inflammation in colitis by scavenging ROS and regulating macrophage M2 polarization. *Int J Nanomedicine* **18**, 4601–4616 (2023).

[63] Yang, H.; Sun, A.; Yang, J.; Cheng, H.; Yang, X.; Chen, H.; Falahati, M. Development of doxorubicin-loaded chitosan–heparin nanoparticles with selective anticancer efficacy against gastric cancer cells in vitro through regulation of intrinsic apoptosis pathway. *Arab J Chem* **14**, 103266 (2021).

[64] Dong, L.; Li, M.; Zhang, S.; Li, J.; Shen, G.; Tu, Y.; Zhu, J.; Tao, J. Cytotoxicity of bovine serum albumin-stabilized gold nanoclusters: in vitro and in vivo study. *Small* **11**, 2571–2581 (2015).

[65] Kciuk, M.; Gielecińska, A.; Mujwar, S.; Kołat, D.; Kałuzińska-Kołat, Ż.; Celik, I.; Kontek, R. Doxorubicin—an agent with multiple mechanisms of anticancer activity. *Cells* **12**, 659 (2023).

[66] Liu, J.; Cabral, H.; Mi, P. Nanocarriers address intracellular barriers for efficient drug delivery, overcoming drug resistance, subcellular targeting and controlled release. *Adv Drug Deliv Rev* **207**, 115239 (2024).

[67] Alshawwa, S. Z.; Kassem, A. A.; Farid, R. M.; Mostafa, S. K.; Labib, G. S. Nanocarrier drug delivery systems: characterization, limitations, future perspectives and implementation of artificial intelligence. *Pharmaceutics* **14**, 883 (2022).

[68] Chen, L.; Hong, W.; Ren, W.; Xu, T.; Qian, Z.; He, Z. Recent progress in targeted delivery vectors based on biomimetic nanoparticles. *Signal Transduct Target Ther* **6**, 225 (2021).

[69] Weeratunga, S.; Paul, B.; Collins, B. M. Recognising the signals for endosomal trafficking. *Curr Opin Cell Biol* **65**, 17–27 (2020).

[70] Li, X.; Garrity, A. G.; Xu, H. Regulation of membrane trafficking by signalling on endosomal and lysosomal membranes. *J Physiol* **591**, 4389–4401 (2013).

[71] Desai, N.; Rana, D.; Salave, S.; Benival, D.; Khunt, D.; Prajapati, B. G. Achieving endo/lysosomal escape using smart nanosystems for efficient cellular delivery. *Molecules* **29**, 3131 (2024).

[72] Tang, R.; Ye, Y.; Zhu, S.; Wang, Y.; Lu, B.; Yao, Y. Pillar[6]arenes: from preparation and host–guest properties to self-assembly and applications. *Chin Chem Lett* **34**, 107734 (2023).